Non-thermal breaking of magnetic order via photo-generated spin defects

Ernest Pastor[1†], David Moreno-Mencía[1†], Maurizio Monti[2], Allan S. Johnson[1], Nina Fleischmann[1], Cuixiang Wang[3], Youguo Shi[3], Xuerong Liu[4], Daniel G. Mazzone[5], Mark P.M. Dean[6], Simon Wall[*1,2]*

[1] *ICFO-Institut de Ciències Fotòniques, The Barcelona Institute of Science and Technology, 08860, Castelldefels, Barcelona, Spain.*

[2]*Department of Physics and Astronomy, Aarhus University, Ny Munkegade 120, 8000 Aarhus C, Denmark.*

[3]*Beijing National Laboratory for Condensed Matter Physics, Institute of Physics, Chinese Academy of Sciences, Beijing 100190, China*

[4] *School of Physical Science and Technology, ShanghaiTech University, Shanghai 201210, China.*

[5] *Laboratory for Neutron Scattering and Imaging, Paul Scherrer Institut, CH-5232 Villigen, Switzerland*

[6] *Condensed Matter Physics and Materials Science Department, Brookhaven National Laboratory, Upton, New York 11973, USA.*

[†]*Equal contribution*

**Corresponding authors: ernest.pastor@icfo.eu, simon.wall@phys.au.dk*

In Mott insulators the evolution of antiferromagnetic order to superconducting or charge-density-wave-like states upon chemical doping underpins the control of quantum phases. Photo-doping can induce similar transitions on the ultrafast timescale, however the response of the spin system has remained elusive. Here, we use 4D-ultrafast optical

spectroscopy to extract quantitative magnetic dynamics in the spin-orbit coupled Mott insulator $Sr_3Ir_2O_7$. We demonstrate that light can non-thermally melt long-range spin order. At low fluences magnetic order recovers within 1 ps despite demagnetization of roughly 50%. However, high fluences induce a crossover to a long-lived demagnetized state without increasing the lattice temperature. We show that the generation of photo-induced spin defects enables a mechanism that stabilizes the demagnetized state which could help expose new transient phases.

In Mott insulators, the breakdown of long-range antiferromagnetic spin order into phases such as high-temperature superconductivity through doping is a key method to control quantum materials in equilibrium(*1*, *2*). Out of equilibrium, the use of light has emerged as a powerful tool to access new phases, but the role played by the spin degree of freedom in these processes remains poorly understood. Antiferromagnetic order is particularly challenging to track and this has stimulated the development of new methods to probe it on fast timescales (*2–10*). However, while these probes have shown that magnetic order in Mott insulators can be suppressed on the ultrafast timescale, they often lack sensitivity to other degrees of freedom preventing deeper insights into how order breaking unfolds. In particular, it remains unknown if optical quenching of the spin order requires a concomitant heating of the lattice, i.e. if the suppression of spin order is due to rapid, but trivial, heating, or if in contrast, the suppression is non-thermal, potentially enabling access to new transient states unreachable in thermodynamic equilibrium. Whether the process occurs thermally or non-thermally is critical as it dictates what mechanism stabilizes the photoexcited state, and ultimately determines our ability to control it.

Herein we record the transient optical response of a correlated antiferromagnetic Mott insulator in four dimensions namely, as a function of time, wavelength, excitation fluence and temperature. This multidimensional approach allows us to separate out magnetic dynamics

from structural and electronic processes enabling us to map out quantitative magnetic changes in unprecedented detail, while also assessing the lattice temperature from the viewpoint of the phonon frequencies. We focus on an iridium-based oxide, which has a strong spin-orbit coupling (SOC) and similarities to superconducting curates (*11–13*). We show that in this system, moderate phot-excitations causes a large, ~50%, and prompt suppression of magnetic order which can recover rapidly (under a picosecond). In contrast at higher excitation densities, the magnetic order can be completely suppressed, resulting in a dramatic increase of the recovery time. Crucially, we demonstrate that the lattice temperature remains below the equilibrium Néel temperature (T_N) while the system is in the demagnetized state, showing that the long-lived state is non-thermal. Our experiments and simulations suggest that the formation of photo-induced spin defects dictates the stability of the demagnetized state and the recovery of magnetic order. The picture that emerges from our data is one in which system disorder plays a dominant role in determining the fate of the photo-excited state offering an opportunity to tune antiferromagnetic order without changing the temperature and ultimately achieve new functionality.

$Sr_3Ir_2O_7$ exhibits an antiferromagnetic to paramagnetic transition at T_N~280 K (*14*). Due to the slater-like element of the band gap, a noticeable change in resistance occurs below T_N despite the system remaining gapped. These changes are also observed in the optical conductivity and thus in the reflectivity. In particular, the visible spectral region probes transitions involving lower-lying O 2p and Ir 5d states to unoccupied states near the band gap (*15*, *16*) resulting in magnetic sensitivity. Indeed, the static reflectivity significantly increases above T_N (Fig. 1A). While the reflectivity shows sensitivity to magnetic order, it also depends on the electronic and structural degrees of freedom. As these also evolve with temperature, isolating the magnetic signal is non-trivial and hinders accurate quantification of the magnetic order from the reflectivity alone.

This challenge can, however, be overcome with ultrafast broadband spectroscopy. By analyzing the temperature dependence of the transient spectral shifts, we can identify regions of the spectra that are dominated by the magnetic signal. Fig.1B shows typical broadband transient reflectivity spectra taken above and below T_N, following photoexcitation with 800 nm (1.5eV, F = 5 $mJcm^{-2}$) laser light (other fluences displayed in Fig. S2). The spectral changes are qualitatively similar in both cases. Both temperatures show a suppressed reflectivity at short wavelengths and a signal enhancement above ~600 nm (see lineouts in Fig.1B) consistent with a shift in the O2p-Ir5d charge transfer resonance (*17*). Moreover they both exhibit fast dynamics within the first picosecond, followed by a much slower plateau. The signal is also modulated by an oscillating component due to coherent phonons.

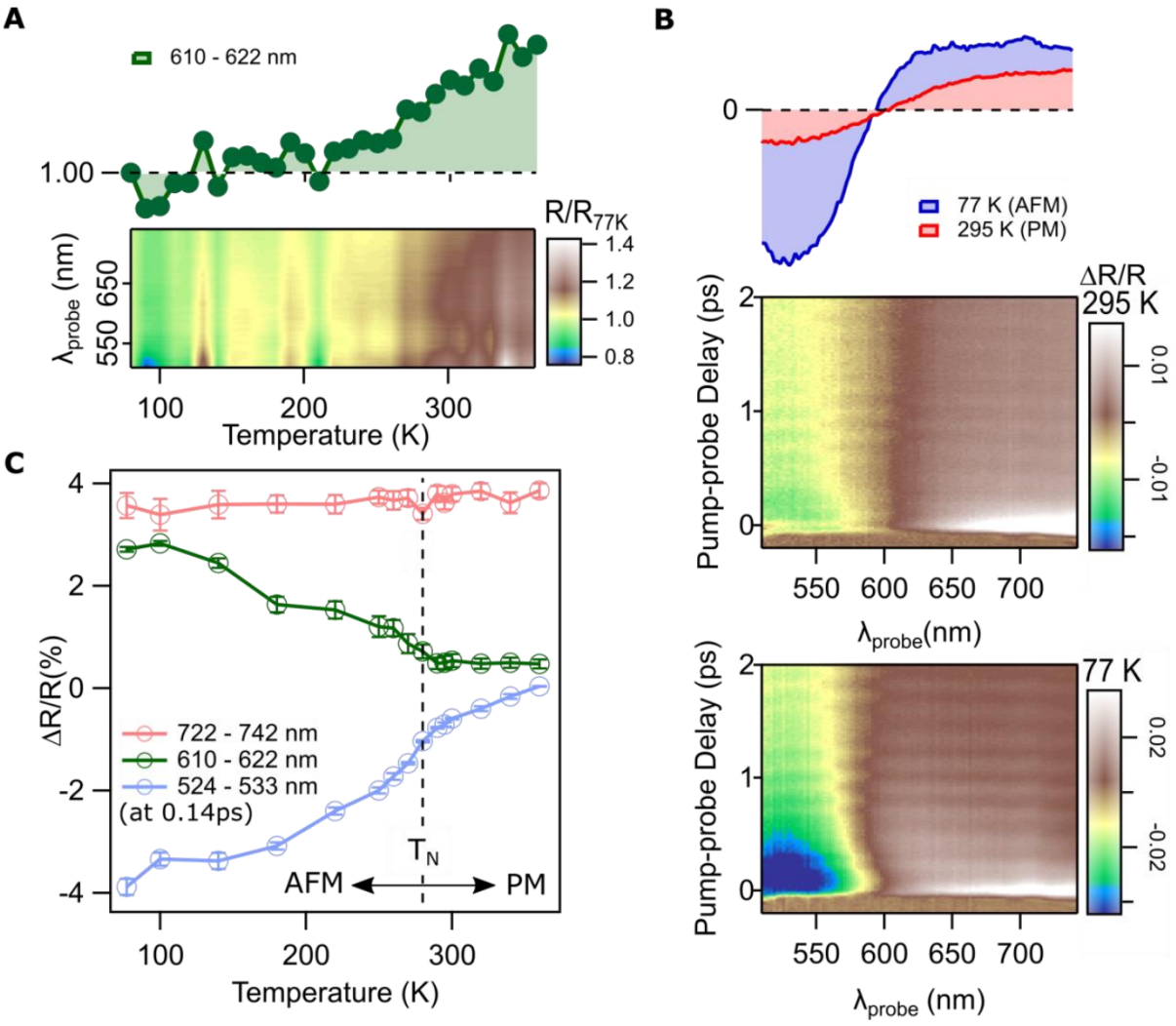

Fig. 1: Magnetic and electronic changes in $Sr_3Ir_2O_7$. (A) Temperature dependence of the static reflectivity. The signal is shown relative to the value at 77 K (AFM). Top: Lineout at ~610 nm showing a change in reflectivity between low and high temperatures. For clarity the signal is smoothed; raw data are displayed in Fig. S1. (B) Transient reflectivity change upon 800 nm excitation (F = 5 $mJcm^{-2}$) at 77 K (antiferromagnetic, AFM) and 295 K (paramagnetic, PM). Top: lineout at 0.14 ps time delay. (C) Temperature dependence of the transient reflectivity at different probe wavelengths. For clarity the traces are offset. The 610 nm region is both sensitive to magnetic order while showing a temperature independent response above T_N.

At room temperature, where the system has no magnetic order, the dynamics result from purely electronic and structural changes. Below T_N, the spectral response is similar, but with a different magnitude. In particular, we observe a significant signal enhancement around 500-650 nm, while the changes above 650 nm are less abrupt. In addition, we also observe a change in the amplitude and the central frequency of the coherent phonons with increasing temperature, as discussed later. While these differences between low (AFM) and high (PM) temperatures indicate a fingerprint of magnetic behavior, it remains unclear whether the observed optical signals can be attributed exclusively to the magnetic degrees of freedom.

To establish which region has the most sensitivity to magnetic order and least sensitivity to the other degrees of freedom, we measure a 4D dataset, recording the response of the system as a function of probe wavelength, λ, fluence, F, temperature, T, and time, t. In detail, our aim is to identify a region of the spectra that is most insensitive to thermal changes in the electronic and structural properties above T_N. This allows us to subsequently subtract these contributions from the signal below T_N and thus to isolate the magnetic response. Fig.1C shows a detailed temperature scan at different probe wavelengths for a fixed fluence and delay, which exemplifies the merits of our approach. From the data in Fig. 1B alone (comparison of spectra at 295 K and 77 K), one might assume that the 500-550 nm region would exhibit the largest magnetic sensitivity as it shows the largest change when crossing T_N. However, the full temperature scan reveals that this region is strongly temperature dependent above T_N, which precludes extraction of the magnetic signal without a detailed understanding of the non-magnetic temperature evolution of the system. Likewise, at long wavelengths (> 700 nm) the signal shows a temperature independent response above T_N, but lacks magnetic sensitivity. Between these two extremes, we find that wavelengths around 610 nm are unique because the electronic response is temperature independent above T_N, whilst retaining sensitivity to

magnetic order. This remains true for all probed fluences and time delays as shown in Fig. S3 and as discussed below.

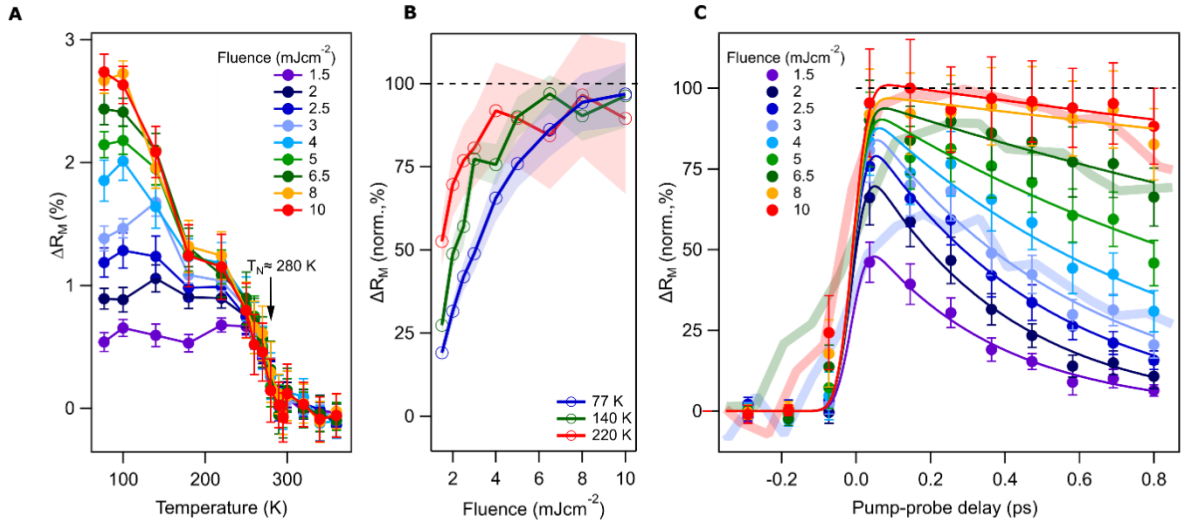

Fig. 2: Ultrafast changes in magnetic order: (A) Temperature dependence of the magnetic degree of freedom (ΔR_M) at different excitation fluences measured at 360 fs time delay obtained as $\Delta R(T)$- $\Delta R(T>T_N)$ in the 610 nm region. The signal saturates at high fluences and at temperatures close the Néel temperature as expected for light-induced demagnetization. We normalize the maximum ΔR_M value at 10mJ cm^{-2} to 100% demagnetization. (B) Fluence dependence of the magnetic signal at different temperatures showing that full demagnetization is more rapidly attained at higher temperatures. (C) Time-evolution of the magnetic signal measured at 77 K at different fluences showing fast and large (>40%) demagnetization as well a change from rapid recovery to permanent demagnetization at F > 4 mJ cm^{-2}. For comparison, the time evolution of the magnetic Bragg peak obtained from (*12*) is also shown (solid translucent lines, scaled).

Fig. 2A shows the magnitude of the reflectivity change after subtracting the electronic contribution from the total reflectivity ($\Delta R(T)$- $\Delta R(T>T_N)$) at 610 nm and 360 fs time delay.

We label this assay of magnetism as ΔR_M (see Fig. 2C and Fig. S4 for other time delays and details). Above T_N the signal is zero at all fluences, as expected from our methodology. At T_N there is a discontinuity and the magnetic response rises sharply for all fluences. The magnetic signal continues to grow for high pump intensities as the sample is cooled, whereas at lower fluences ($F < 3$mJ cm^{-2}) the signal remains flat. Notably, at lower temperatures, larger changes can be induced before saturation, which also requires higher fluences to be reached (see Fig. 2B). Such behavior suggests that as the temperature is lowered and the system becomes more ordered, more energy is needed to perturb it and to demagnetize it. Based on this, we assign the saturation fluence as the fluence required to completely suppress magnetic order. For all temperatures we observe that fluences above ~4-5 mJcm^{-2} result in saturation. Thus, we normalize ΔR_M to the value obtained at the highest excitation fluence (F = 10 mJcm^{-2}), which provides a scale for a quantitative analysis of the demagnetization.

Next, we analyze the demagnetization dynamics. Fig. 2C shows the change in the normalized magnetic signal at 77 K when the sample is in the antiferromagnetic state. We observe a sharp change in the magnetic signal immediately after photoexcitation. Notably, we find a very large (>50%) demagnetization even at low fluences, which is a strong indicator that the magnetic order can be efficiently perturbed by the laser pulse in this material. For comparison, we overlay the time evolution of a magnetic Bragg peak measured at several (high) fluences using XFEL radiation (*12*). The differences between the two experimental conditions prevent exactly matching the fluences (see Supporting Information), but the agreement between the optical and x-ray data is remarkable providing further confirmation that our optical signal is a robust assay of changes in the magnetic order.

Following this initial demagnetization step, we distinguish two regimes in our data: (i) below a threshold fluence F^{th} ~4-5 mJcm^{-2} the signal decays and recovers rapidly; the timescale of such re-magnetization is strongly fluence dependent. (ii) Above F^{th} the signal saturates and

exhibits a minimal decay within 1 ps, indicating near-complete and permanent demagnetization. The observation of the two regimes, and separating threshold fluence, suggests that laser radiation can access different mechanisms of de- and re-magnetization in the material. Fig. 3A shows the fluence threshold required to switch between demagnetization regimes as a function of temperature. Red regions correspond to parameters which result in at least a 50% recovery of the magnetic order within 1 ps, whereas blue regions show long-lived demagnetization. The cross-over fluence threshold at 77 K is approximately 4mJ cm^{-2} and decreases with increasing temperature so that above ~200 K only the long-lived de-magnetized state remains.

These results may be explained by a multi-temperature model in which the spin system is quickly heated via the laser excitation and followed by a subsequent cooling through a transfer of heat to the lattice (*18*). In this scenario, the long-lived demagnetized state arises simply because the lattice temperature has risen above T_N. To test this hypothesis, we probed the lattice temperature by taking advantage of the strongly temperature dependent A_{1g} phonon modes (*19*). Using time-resolved coherent phonon spectroscopy, we compared the photo-induced A_{1g} phonon modes with those measured a room temperature. High time-resolution scans were performed at room temperature and at 77 K (see Fig. 1B and supplementary materials for details). Both ~147 cm^{-1} and ~181 cm^{-1} A_{1g} modes can be clearly resolved in the broadband data and red shift at higher temperature (Fig. 3B). The values obtained at low excitation fluence are in good agreement with those measured with equilibrium Raman spectroscopy, indicating that low fluence excitation does not significantly heat the system (*14*). In order to assess the lattice temperature as a function of excitation fluence, we measure the phonon frequencies at 77 K. Although both A_{1g} modes show a gradual red shift with fluence, as expected for heating, we find that the red shift is significantly smaller than that when the system had crossed T_N (Fig. 3C). In particular, at the magnetic crossover threshold ($F^{th.}$) the phonon values are only

moderately perturbed, suggesting that a lattice temperature increase is not required to either suppress long-range spin order, nor prevent its recovery.

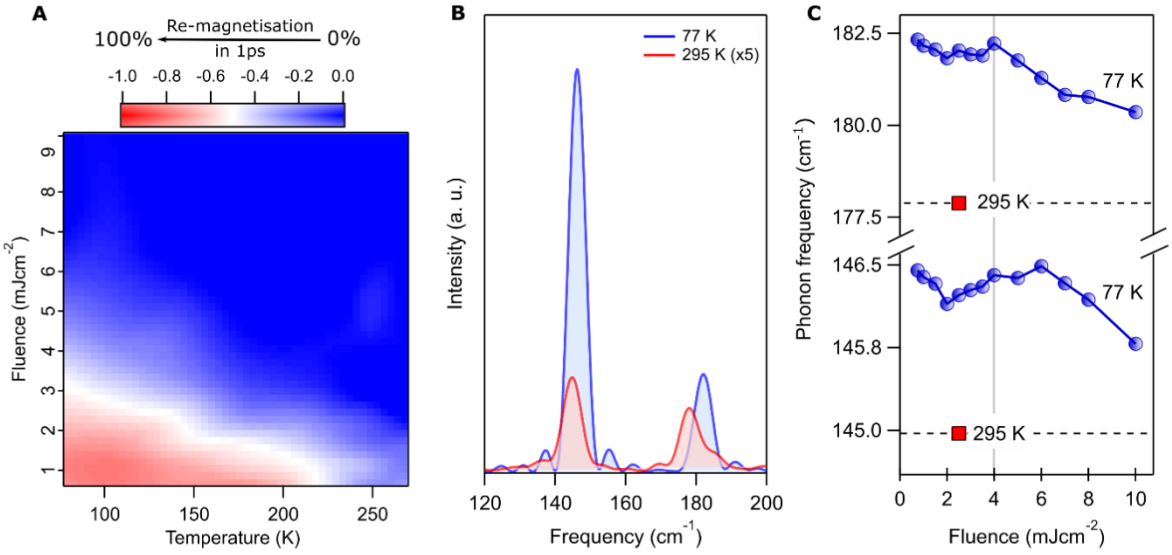

Fig. 3: Non- thermal crossover between re-magnetization domains. (A) Fluence and temperature dependence of the re-magnetization dynamics. The plot shows the extent to which the magnetic signal (ΔR_M) recovers (i.e.: decay in Fig. 2C) between the initial excitation t = 0 ps and a delay of 1 ps. The crossover between fast recovery (red) and persistent signal (blue) decreases as the temperature approaches T_N. (B) Fourier Transform of the oscillations in the transient reflectivity at 77 K (AFM) and 295 K (PM) at F = 2.5 mJcm^{-2}. The characteristic high and low energy A_{1g} modes can be captured. The amplitude decreases and the central frequency red shifts with increasing temperature. (C) Change in the mode frequency as a function of excitation fluence at 77 K (AFM). For comparison the frequency measured at 295K (PM) at low fluences is also displayed (red square). Despite large demagnetization achieved at all fluences, the modes remain mostly unchanged and exhibit only a small inflection at the crossover fluence threshold (F^{th}) but never reach the thermal value.

Our observations can be explained by considering how photo-excitation modifies magnetic order in insulating quantum materials with strong spin-orbit coupling (SOC). Optical excitation creates electron-hole pairs causing changes in orbital occupancies. Due to the small charge gap in $Sr_3Ir_2O_7$, it is energetically favorable to create zero-spin doubly occupied sites following photoexcitation effectively generating 'spin defects' in the system (Fig. 4A) (*13*). This configuration is unstable and at low excitation density the excited electron can recombine with its corresponding hole via the emission of phonons. Although it is in principle possible for any electron to recombine with any available hole (leading for example to hole motion), the strong exchange coupling, which is only slightly smaller than the charge gap, disfavors an electron from recombining with a hole that does not result in antiparallel spin alignment. This is depicted in Fig. 4A and B. If the electron-hole pair recombine before the surrounding spin system has time to react, the magnetic order can be restored without disordering the spin system beyond the initial creation of the spin defects. This suggests a direct link between electrons rapidly relaxing back to the valence band and the fast recovery of magnetic order, as measured at low excitation fluences. We indeed observe that the magnetic recovery in such a regime and the electronic relaxation times measured above T_N are comparable, suggesting electron-hole recombination in the low-density limit can restore the initial spin configuration. Notably, this process is markedly non-thermal as shown by the coherent phonon analysis and represents magnetic perturbations beyond linear spin-wave theory. At higher excitation fluences, a large density of spin defects is created, as depicted in Fig. 4C. When these defects are close, the energy barrier preventing electron-hole recombination events that result in non-antiparallel spin alignments is significantly reduced. This result in a mixture of parallel and antiparallel spin alignments that eventually disorders the underlying spin network, slowing down the regeneration of the long-range order.

To test the feasibility of this scenario, we examine the recovery of a 3D spin-1/2 Ising model following a change in the magnetic order using a Monte Carlo simulation. We assume the creation of doubly occupied sites can be simplified as direct spin flips, with the flipping fraction depending on the laser fluence. We then count how many Monte-Carlo steps are required to return to the equilibrium conditions (Fig. 4D). When the spin network is only weakly perturbed, order recovers quickly. However, when the system approaches complete demagnetization, the recovery slows down dramatically and the system remains demagnetized, despite the temperature of the simulation being significantly below T_N (see also Fig. S5). This fast recovery at small perturbations and the generation of a long-lived state at high defect concentrations in the absence of system heating is in good agreement with our experimental observations. We note that this basic model does not honor the complexity of $Sr_3Ir_2O_7$. For example, the model is blind to the mechanism of perturbation beyond imposing an instantaneous change, which is something that will depend on the dominant energy scale of the system. Indeed, while charge transfer in any Mott insulator is expected to produce rapid demagnetization (*20*), the exact nature of the spin-orbit coupling and the exchange interaction are likely key factors for explaining the magnitude and speed of the switching process (*21*). Notwithstanding the limitations of the model, this approach allows us to explore the basic response of a system to a disruption of long-range order and highlights the role played by the degeneracy of the spin-disordered state in preventing a rapid recovery. This points towards a central role of disorder in determining the physics of irradiated solids (*22*). While disorder has been largely regarded as undesirable, increasing evidence suggest it might be essential in enabling and controlling functionality in systems such as solar cells and photocatalysts and might provide new paths to control the excited state (*23–25*).

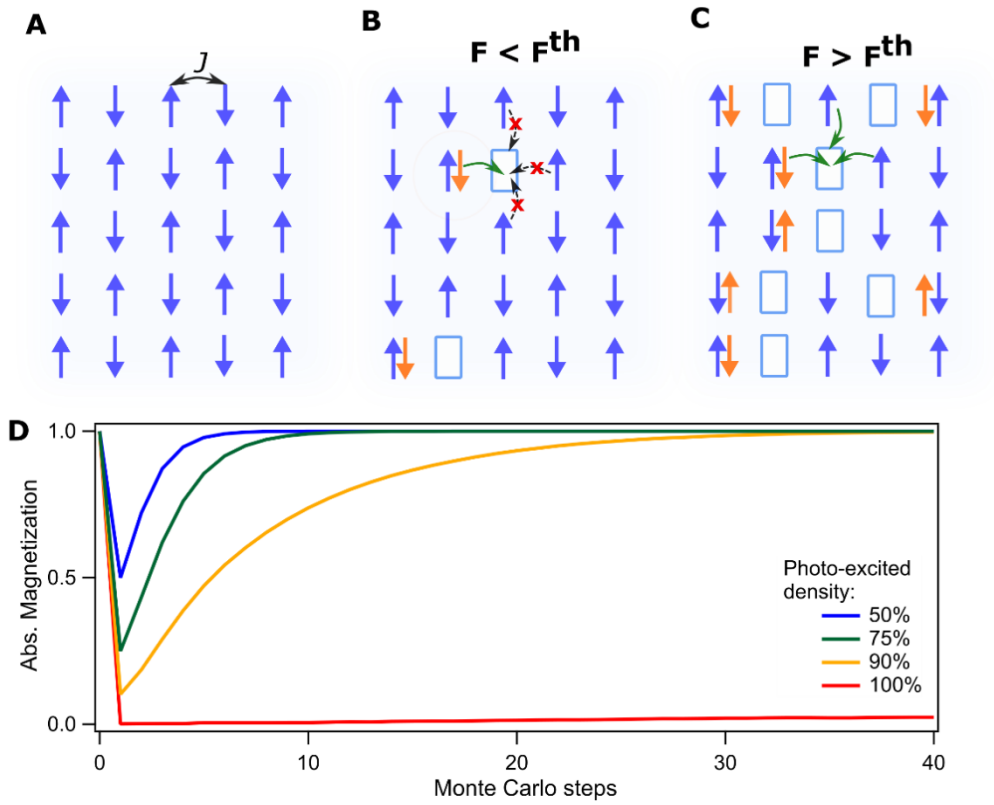

Fig. 4: Disorder mediated recovery of magnetic order. (A) Ground state characterized by a large exchange coupling (*J*) that leads to antiferromagnetic (AFM) order. (B) Photoexcitation below the fluence threshold (F^{th}) results in the formation of a small density of spin vacancies and doubly occupied states with zero net moment. Effective destruction of the moment is enabled by the small charge gap. Rapid recombination events regenerate the antiferromagnetic order but recombination paths that produce parallel spin alignments are prevented by the dominant antiferromagnetic exchange coupling (C) Photoexcitation above the fluence threshold. The formation of a large density of spin vacancies relaxes the recombination constraint leading to a long-lived disordering of the spin system. (D) Monte Carlo Magnetization dynamics in a 3D spin-1/2 Ising model resulting from an instantaneous and random spin flips at different degrees of excitation. If a small fraction of spins is flipped the system recovers fast. In contrast when a large number of spins are flipped inducing large disorder, long-lived change in magnetization occurs.

In summary, we have shown how photo-excitation of $Sr_3Ir_2O_7$ can non-thermally suppress the magnetic long-range order. We have found a regime, at low fluences and low temperatures, in which we are able to manipulate the magnetic order by up to 50%, but where the system can recover within a picosecond. In contrast, at higher fluences we measure a crossover to a regime in which the magnetic order is completely suppressed for long times, but where the lattice temperature remains below T_N. Such crossover emanates from the generation of photoinduced spin defects that enable a pathway for spin disordering and long-lived breaking of magnetic order. The light-induced, non-thermal change of spin order opens new opportunities to investigate transient phases in solids. In particular, the iridates have long been thought of as the 5d analogues of cuprates, but the disruption of magnetic order through static doping did not allow to induce superconductivity. Optical excitation and manipulation of long-lived spin order might enable a new route to access and stabilize superconductivity.

Acknowledgements

This work was funded through the European Research Council (ERC) under the European Union's Horizon 2020 Research and Innovation Programme (Grant Agreement No. 758461), by the Ministry of Science, Innovation and Universities (MCIU), State Research Agency (AEI) and European Regional Development Fund (FEDER) PGC2018-097027-B-I00, the Spanish State Research Agency through the "Severo Ochoa" program for Centers of Excellence in R&D (CEX2019-000910-S), the Fundació Cellex, and Fundació Mir-Puig, the Generalitat de Catalunya through the CERCA program. E.P. and A.S.J acknowledge support from the Marie Skłodowska-Curie co-fund a PROBIST fellowship (grant agreement No. 754510). E.P also thanks the Spanish Ministry of Science for a Juan de la Cierva contract (IJC2018-037384-I).

X.L. acknowledges support from the National Natural Science Foundation of China under grant No. 11934017. Work at Brookhaven National Laboratory was supported by the U.S. Department of Energy, Office of Science, Office of Basic Energy Sciences under Contract No. DE-SC0012704. C.W. and Y. S. acknowledge the support from the National Natural Science Foundation of China (Grants No. U2032204) and the K. C. Wong Education Foundation (GJTD-2018-01).

References

1. P. A. Lee, N. Nagaosa, X.-G. Wen, Doping a Mott insulator: Physics of high-temperature superconductivity. *Rev. Mod. Phys.* **78**, 17–85 (2006).

2. D. N. Basov, R. D. Averitt, D. Hsieh, Towards properties on demand in quantum materials. *Nat. Mater.* **16**, 1077–1088 (2017).

3. M. P. M. Dean, Y. Cao, X. Liu, S. Wall, D. Zhu, R. Mankowsky, V. Thampy, X. M. Chen, J. G. Vale, D. Casa, J. Kim, A. H. Said, P. Juhas, R. Alonso-Mori, J. M. Glownia, A. Robert, J. Robinson, M. Sikorski, S. Song, M. Kozina, H. Lemke, L. Patthey, S. Owada, T. Katayama, M. Yabashi, Y. Tanaka, T. Togashi, J. Liu, C. Rayan Serrao, B. J. Kim, L. Huber, C.-L. Chang, D. F. McMorrow, M. Först, J. P. Hill, Ultrafast energy- and momentum-resolved dynamics of magnetic correlations in the photo-doped Mott insulator Sr2IrO4. *Nat. Mater.* **15**, 601–605 (2016).

4. T. Kampfrath, A. Sell, G. Klatt, A. Pashkin, S. Mährlein, T. Dekorsy, M. Wolf, M. Fiebig, A. Leitenstorfer, R. Huber, Coherent terahertz control of antiferromagnetic spin waves. *Nat. Photonics*. **5**, 31–34 (2011).

5. V. G. Sala, S. Dal Conte, T. A. Miller, D. Viola, E. Luppi, V. Véniard, G. Cerullo, S. Wall, Resonant optical control of the structural distortions that drive ultrafast demagnetization in Cr2O3. *Phys. Rev. B*. **94**, 014430 (2016).

6. M. Först, R. I. Tobey, S. Wall, H. Bromberger, V. Khanna, A. L. Cavalieri, Y. D. Chuang, W. S. Lee, R. Moore, W. F. Schlotter, J. J. Turner, O. Krupin, M. Trigo, H. Zheng, J. F. Mitchell, S. S. Dhesi, J. P. Hill, A. Cavalleri, Driving magnetic order in a manganite by ultrafast lattice excitation. *Phys. Rev. B*. **84**, 241104 (2011).

7. D. Afanasiev, A. Gatilova, D. J. Groenendijk, B. A. Ivanov, M. Gibert, S. Gariglio, J. Mentink, J. Li, N. Dasari, M. Eckstein, T. Rasing, A. D. Caviglia, A. V. Kimel, Ultrafast Spin Dynamics in Photodoped Spin-Orbit Mott Insulator Sr2IrO4. *Phys. Rev. X*. **9**, 021020 (2019).

8. K. R. Beyerlein, A. S. Disa, M. Först, M. Henstridge, T. Gebert, T. Forrest, A. Fitzpatrick, C. Dominguez, J. Fowlie, M. Gibert, J.-M. Triscone, S. S. Dhesi, A. Cavalleri, Probing photoinduced rearrangements in the NdNiO3 magnetic spiral with polarization-sensitive ultrafast resonant soft x-ray scattering. *Phys. Rev. B*. **102**, 014311 (2020).

9. Y. D. Chuang, W. S. Lee, Y. F. Kung, A. P. Sorini, B. Moritz, R. G. Moore, L. Patthey, M. Trigo, D. H. Lu, P. S. Kirchmann, M. Yi, O. Krupin, M. Langner, Y. Zhu, S. Y. Zhou, D. A. Reis, N. Huse, J. S. Robinson, R. A. Kaindl, R. W. Schoenlein, S. L. Johnson, M. Först, D. Doering, P. Denes, W. F. Schlotter, J. J. Turner, T. Sasagawa, Z. Hussain, Z. X. Shen, T. P. Devereaux, Real-Time Manifestation of Strongly Coupled Spin and Charge Order Parameters in Stripe-Ordered La1.75Sr0.25NiO4 Nickelate Crystals Using Time-Resolved Resonant X-Ray Diffractio. *Phys. Rev. Lett.* **110**, 127404 (2013).

10. S. L. Johnson, R. A. de Souza, U. Staub, P. Beaud, E. Möhr-Vorobeva, G. Ingold, A. Caviezel, V. Scagnoli, W. F. Schlotter, J. J. Turner, O. Krupin, W.-S. Lee, Y.-D. Chuang, L. Patthey, R. G. Moore, D. Lu, M. Yi, P. S. Kirchmann, M. Trigo, P. Denes, D. Doering, Z. Hussain, Z.-X. Shen, D. Prabhakaran, A. T. Boothroyd, Femtosecond Dynamics of the Collinear-to-Spiral Antiferromagnetic Phase Transition in CuO. *Phys. Rev. Lett.* **108**, 037203 (2012).

11. J. Bertinshaw, Y. K. Kim, G. Khaliullin, B. J. Kim, Square Lattice Iridates. *Annu. Rev. Condens. Matter Phys.* **10**, 315–336 (2019).

12. D. G. Mazzone, D. Meyers, Y. Cao, J. G. Vale, C. D. Dashwood, Y. Shi, A. J. A. James, N. J. Robinson, J. Q. Lin, V. Thampy, Y. Tanaka, A. S. Johnson, H. Miao, R. Wang, T. A. Assefa, J. Kim, D. Casa, R. Mankowsky, D. Zhu, R. Alonso-Mori, S. Song, H. Yavas, T. Katayama, M. Yabashi, Y. K. S. Owada, J. Liu, J. Yang, R. M. Konik, I. K. Robinson, J. P. Hill, D. F. McMorrow, M. Forst, S. Wall, X. Liu, M. P. M. Dean, Trapped Transient Magnons in the Gapped Antiferromagnet Sr3Ir2O7. *arXiv* (2020).

13. J. Kim, A. H. Said, D. Casa, M. H. Upton, T. Gog, M. Daghofer, G. Jackeli, J. van den Brink, G. Khaliullin, B. J. Kim, Large Spin-Wave Energy Gap in the Bilayer Iridate e Sr3Ir2O7: Evidence for Enhanced Dipolar Interactions Near the Mott Metal-Insulator Transition. *Phys. Rev. Lett.* **109**, 157402 (2012).

14. H. Gretarsson, N. H. Sung, M. Höppner, B. J. Kim, B. Keimer, M. Le Tacon, Two-Magnon Raman Scattering and Pseudospin-Lattice Interactions in Sr2IrO4 and Sr3Ir2 O7. *Phys. Rev. Lett.* **116**, 17–20 (2016).

15. P. Liu, B. Kim, X. Q. Chen, D. D. Sarma, G. Kresse, C. Franchini, Relativistic GW +BSE study of the optical properties of Ruddlesden-Popper iridates. *Phys. Rev. Mater.*

2, 075003 (2018).

16. H. J. Park, C. H. Sohn, D. W. Jeong, G. Cao, K. W. Kim, S. J. Moon, H. Jin, D.-Y. Cho, T. W. Noh, Phonon-assisted optical excitation in the narrow bandgap Mott insulator Sr3Ir2 O7. *Phys. Rev. B*. **89**, 155115 (2014).

17. A. Ramos-Alvarez, N. Fleischmann, L. Vidas, A. Fernandez-Rodriguez, A. Palau, S. Wall, Probing the lattice anharmonicity of superconducting YBa2Cu3O7−δ via phonon harmonics. *Phys. Rev. B*. **100**, 184302 (2019).

18. B. Koopmans, G. Malinowski, F. Dalla Longa, D. Steiauf, M. Fähnle, T. Roth, M. Cinchetti, M. Aeschlimann, Explaining the paradoxical diversity of ultrafast laser-induced demagnetization. *Nat. Mater.* **9**, 259–265 (2010).

19. L. L. Hu, M. Yang, Y. L. Wu, Q. Wu, H. Zhao, F. Sun, W. Wang, R. He, S. L. He, H. Zhang, R. J. Huang, L. F. Li, Y. G. Shi, J. Zhao, Strong pseudospin-lattice coupling in Sr3Ir2O7 : Coherent phonon anomaly and negative thermal expans. *Phys. Rev. B*. **99**, 094307 (2019).

20. N. Bittner, D. Golež, H. U. R. Strand, M. Eckstein, P. Werner, Coupled charge and spin dynamics in a photo-excited Mott insulator. *Phys. Rev. B*. **97**, 235125 (2018).

21. J. Li, N. Dasari, M. Eckstein, Ultrafast dynamics in relativistic Mott insulators (2020) arXiv:2010.09253.

22. S. Wall, S. Yang, L. Vidas, M. Chollet, J. M. Glownia, M. Kozina, T. Katayama, T. Henighan, M. Jiang, T. A. Miller, D. A. Reis, L. A. Boatner, O. Delaire, M. Trigo, Ultrafast disordering of vanadium dimers in photoexcited VO 2. *Science (80-.).* **362**, 572–576 (2018).

23. E. Pastor, J.-S. Park, L. Steier, S. Kim, M. Grätzel, J. R. Durrant, A. Walsh, A. A.

Bakulin, In situ observation of picosecond polaron self-localisation in α-Fe2O3 photoelectrochemical cells. *Nat. Commun.* **10**, 3962 (2019).

24. B. Guzelturk, T. Winkler, T. W. J. Van de Goor, M. D. Smith, S. A. Bourelle, S. Feldmann, M. Trigo, S. W. Teitelbaum, H.-G. Steinrück, G. A. de la Pena, R. Alonso-Mori, D. Zhu, T. Sato, H. I. Karunadasa, M. F. Toney, F. Deschler, A. M. Lindenberg, Visualization of dynamic polaronic strain fields in hybrid lead halide perovskites. *Nat. Mater.* (2021), doi:10.1038/s41563-020-00865-5.

25. A. Simonov, A. L. Goodwin, Designing disorder into crystalline materials. *Nat. Rev. Chem.* **4**, 657–673 (2020).

26. L. Li, P. P. Kong, T. F. Qi, C. Q. Jin, S. J. Yuan, L. E. DeLong, P. Schlottmann, G. Cao, Tuning the Jeff=1/2 insulating state via electron doping and pressure in the double-layered iridate Sr3Ir2O7. *Phys. Rev. B*. **87**, 235127 (2013).

27. H. Christiansen, S. Majumder, W. Janke, Phase ordering kinetics of the long-range Ising model. *Phys. Rev. E*. **99**, 011301 (2019)

28. S. Marais, V. Heine, C. Nex, E. Salje, Phenomena due to strain coupling in phase transitions. *Phys. Rev. Lett.* **66**, 2480–2483 (1991).

29. S.-H. Lee, J. S. Goh, D. Cho, Origin of the Insulating Phase and First-Order Metal-Insulator Transition in 1T−TaS2. *Phys. Rev. Lett.* **122**, 106404 (2019).

Supplementary Materials

1. Materials and Methods

Materials: $Sr_3Ir_2O_7$ single crystals were synthesized using the self-flux flux method as described in Reference (*26*) and references therein.

Ultrafast Transient Reflectivity measurements: (Figure 1B, main text) were performed using a Legend Elite amplifier (Coherent) with 800 nm central wavelength, 40 nm bandwidth a pulse duration of ~35 fs with and an energy of 5 W at 5 kHz repetition rate. The broadband visible probe light was generated by focusing a small fraction of the 800 nm beam onto a sapphire crystal while 800 nm light was mechanically chopped at 2.5 kHz and was used as the pump pulse. The pump energy was adjusted using a half wave plate on a motorized stage capable of rotating the polarization of the beam relative to a Brewster polarizer. Both beams were focused on the sample and to ensure probing of a homogeneously pumped region, the probe size (~ $4 \cdot 10^{-5}$ cm^2) was made smaller than the pump size (~ $2 \cdot 10^{-4}$ cm^2). The changes in the reflectivity of the sample were detected using a commercial Andor Zyla sCMOS camera. The cryogenic measurements were performed using liquid nitrogen cryostat (Oxford Instruments, Optistat DN-V).

Static Reflectivity measurements (Figure 1A, main text) were performed on the same sample used in the pump-probe measurements in the cryostat that was also used for the transient reflectivity measurements. A thermal Tungsten-Halogen lamp (Thorlabs SLS201L) was coupled to a multimode fibre and the output imaged onto the sample using a 4f configuration, with a sub-millimeter spot size and an angle of incidence of a few degrees. The reflected light was collected using a second 4f-lens configuration onto a multimode fibre. A cosine corrector was used to reduce the effect of sample drift on the coupling efficiency, and a camera was used to log the sample position in real time to monitor thermal drift. The final spectrum was collected using a silicon CCD spectrometer with 5s exposures (Avantes AvaSpec-Mini4096CL-UVI10). For clarity Figure 1A (main text) displays the measured reflectivity relative to the value at 77K.

2. Analysis of coherent phonons

The transient reflectivity data shown in Figure 1B (main text) is highly modulated at all probe wavelengths by large amplitude oscillations associated with coherent phonons generated by the pump excitation. To extract the frequency of the oscillations the transient data was first differentiated in order to remove the incoherent exponential decay component. Subsequently a fast Fourier transform (FFT) of the resulting differential map yielded a 2D plot of frequency vs probe wavelength. To avoid any coherent artifact at t ~ 0 ps, the dataset was analyzed only between 0.3 – 5.5 ps. To obtain a higher signal to noise level, the frequency map was average at all wavelength yielded modes at ~147 cm^{-1} and ~181 cm^{-1} (Figure 3B, main text). The values obtained are in good agreement with those measured with equilibrium Raman spectroscopy (*14*) and previous ultrafast optical spectroscopy measurements (*19*). Figure S6 shows the different steps of this analysis performed at 77K and 295K.

In order to ensure the reliability of the methodology, single probe wavelengths were also fitted using:

$$f(t) = A + 0.5 * \left(1 + \mathrm{erf}\left(\frac{t - t_0}{t_r}\right)\right) * \left(B * \exp\left(-\frac{(t - t_0)^2}{t_d^2}\right) + C\right)$$

where A correspond to the $\frac{\Delta R}{R}$ (t<0) value, B is the $\frac{\Delta R}{R}$ (t=0) value, and C is $\frac{\Delta R}{R}$ (t>>0) value. t_r and t_d are the time rise and time decay respectively. The fit was subsequently subtracted from the raw data to isolate the oscillating component. The FFT of the residuals yielded the same results as the methodology described above.

3. Calculation of the magnetic contribution

The transient reflectivity at different delay times (t), probe wavelengths (λ) and fluences (F) shows changes at T_N as $\Delta R=\Delta R(T, \lambda, t, F)=\Delta R_e+\Delta R_M$ where ΔR_M and ΔR_e are the magnetic and non-magnetic (e.g. electronic) contributions respectively. A such, $\Delta R_M=0$ for $T>T_N$. Therefore, ΔR_M can be obtained provided that ΔR_e is known. Ideally, the transient response of the electronic system would be a separable function of the different variables (T, λ, t, F), i.e. $\Delta R_e=f(T)g(\lambda)h(t)k(F)$ allowing the functions $g(\lambda)h(t)k(F)$ to be obtained from the high temperature data ($>T_N$). In such case the behavior of the electron system, f(T), could be obtained below T_N. However, we were unable to reliably separate the dataset into functions of specific variables, and no unique spectral function for the electronic degrees of freedom could be found. Therefore, we bypassed this issue by identifying those wavelengths (λ_{e0}) at which $(d\Delta R_e)/dT(\lambda_{e0})=0$. We found that that the region around $\lambda_{e0}\approx600$ nm fulfilled this condition. Note that ΔR_e is not zero, nor is it a constant as a function of time (Figure S3). We assume that the above criteria remains true at this wavelength below T_N and obtain the magnetic contribution as $\Delta R_M= \Delta R(T<TN,\lambda_{e0},t, F)-\Delta R(T> TN,\lambda_{e0},t, F)$ as shown in Figure S4 and Figure 2 (main text). The validity of this approach is further corroborated by comparison of the optically extracted ΔR_M with the magnetic Bragg peak obtained from reference (*12*).

4. Comparison of XFEL and Optical data

The X-ray data used in Figure 2C (main text) and reported in reference (*12*) was performed under grazing incidence and with a 2 μm pump wavelength, whereas the optical work presented herein is performed at 800 nm and a 45 degree angle of incidence. Differences in absorption and reflection coefficients as well as penetration depth miss-matches prevents directly comparing the amplitude of the change and fluence values. In addition, the base temperature of the XFEL data is known with less precision due to the use of a cryosteam cooling system as opposed to the liquid nitrogen cryostat employed in the optical measurements that allows for fine, controlled changes in temperature. Furthermore, the Magnetic Bragg peak data saturates at a value of ~70% due to the pump probe miss-match between laser and X-rays. This difference should be much smaller at visible wavelengths. Therefore, to correct for this, we scale the magnitude of the X-ray data by a constant factor.

5. Details of the Monte Carlo Calculations

Monte Carlo (MC) algorithms and models are commonly used to study equilibrium processes in a variety of systems in physics and beyond. However, they can also be applied to the investigation of dynamical processes (*27*, *28*). Although it is common to implement more complex models (*29*), in this work we opt for the simplest possible description of an antiferromagnet: the 3D spin-1/2 Ising model with nearest neighbors interaction. We find that this model, in its simplicity, is capable of capturing the essence of the magnetization dynamics after photoexcitation and to qualitatively reproduce the experimental observations.

We model the generation of doubly occupied spin states upon laser excitation as direct spin flips. The modeled system consisted of a 3D simple cubic lattice of lateral size L=100 spins (N=1000000 spins in total). A MC step (MCS) is defined as N attempted spin flips for a system of size N. The system was prepared in a perfectly aligned low temperature state and suddenly disordered at time t=2 MCS by flipping a given percentage of the spins (a percentage calculated from the desired demagnetization value) following a random distribution. After that, the system was let free to evolve for a given number of MC steps. The equilibration was implemented using a Metropolis-Hastings algorithm with Glauber dynamics. At each step the staggered magnetization was measured as the difference of the magnetizations of the two sublattices, which were measured as the sum of all the spins alignment in the sublattice.

In the Monte Carlo dynamics, energy is not conserved. Optical excitation, through spin-flips, increases the energy in the system, but as the magnetic order recovers, the total energy of the system decreases. In a real system this energy would translate to an increase in the temperature. As the probability for spin flips increases with increasing Monte Carlo temperature, it may be expected that such a temperature rise may result in more rapid dynamics as the system can more easily leave local minima. Therefore, a second simulation was performed including an increase in temperature together with the demagnetization. The amplitude of the increase in temperature is proportional to the change in the magnetization. The temperature profile is described by:

$$T = T_O + M \cdot C \cdot (1 - e^{-\frac{t}{\tau}})$$

where $T_0 = 0.33T_N$ is the initial temperature, M is the change in magnetization, $C/T_N = 0.56$ is a proportionality constant, which defines the maximum temperature rise relative to a given demagnetization and can be thought of as a heat capacity which converts the non-thermal demagnetization into a temperature. The choice of C=0.56 ensures that the temperature increases substantially above the initial temperature while remaining lower that the transition temperature. This corresponds to a final temperature of 0.89 T_N which is just below the value at which the phase transition starts to affect the dynamics. t is the time in MCS and τ is the characteristic time of the increase in temperature. τ is set to be 1MCS to roughly match the fast time constant in the low fluence simulation. However, the resulting dynamics did not change if the temperature rise was considered to be a step function in time. The top panel of Figure S5 reports the result of such simulation along with the corresponding temperature profile in the bottom panel. The presence of the temperature change does not affect the magnetization dynamics which looks very similar to those reported in Figure 4 in the main text as long as the lattice temperature remained below T_N.

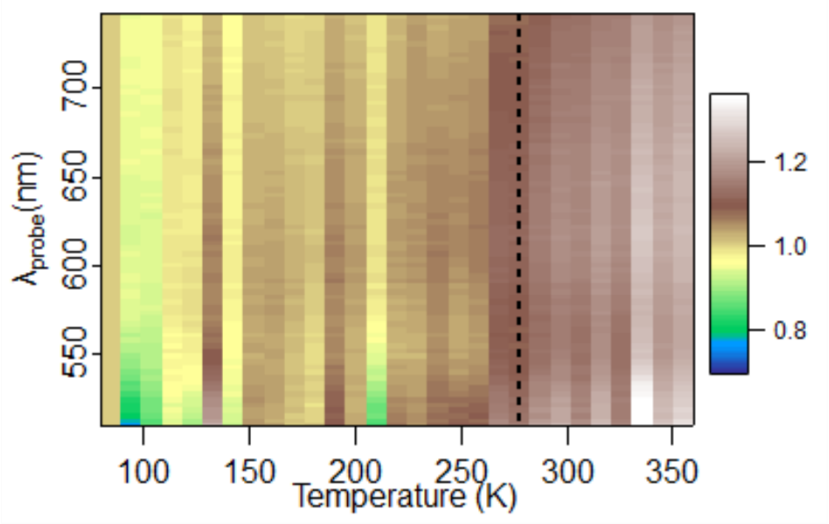

Figure S1: Raw temperature dependence of the static reflectivity which was smoothed in Figure 1A of the main text. The signal is shown relative to the value at 77 K (AFM).

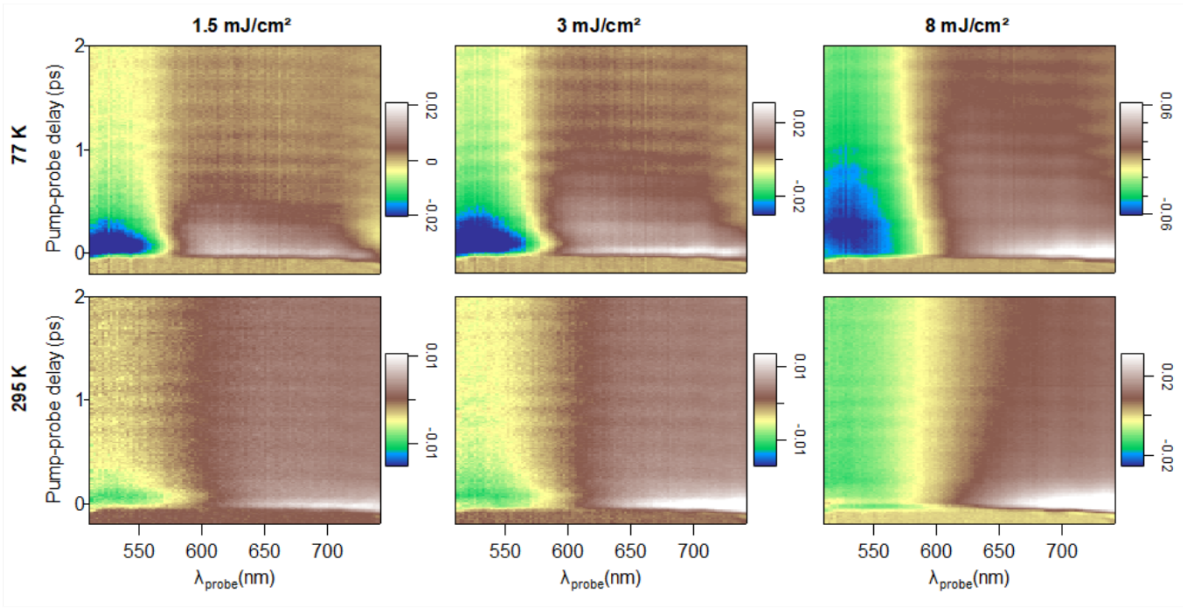

Figure S2: Transient Reflectivity change upon 800nm excitation at 77 K (top) and 295 K (bottom) measured at F = 1.5 mJ cm^{-2}, 3 mJ cm^{-2} and 8 mJ cm^{-2}.

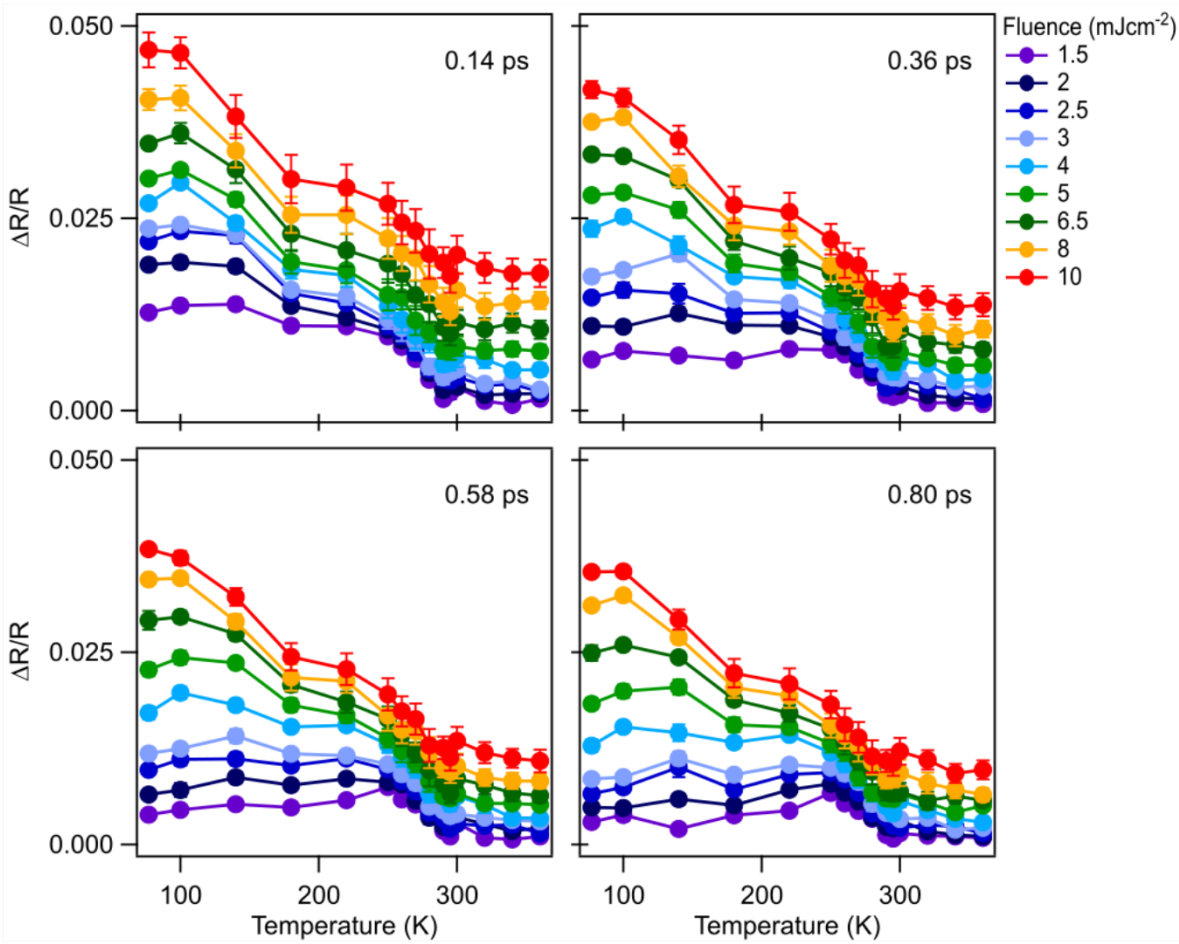

Figure S3: Temperature dependence of the transient reflectivity in the 610-622 nm range at different excitation fluences measured at a time delay of 0.14 ps, 0.36 ps, 0.58 ps and 0.80 ps. This wavelength is both sensitive to magnetic order while showing a temperature independent response above T_N. This behaviour is observed at all measured fluences and time delays.

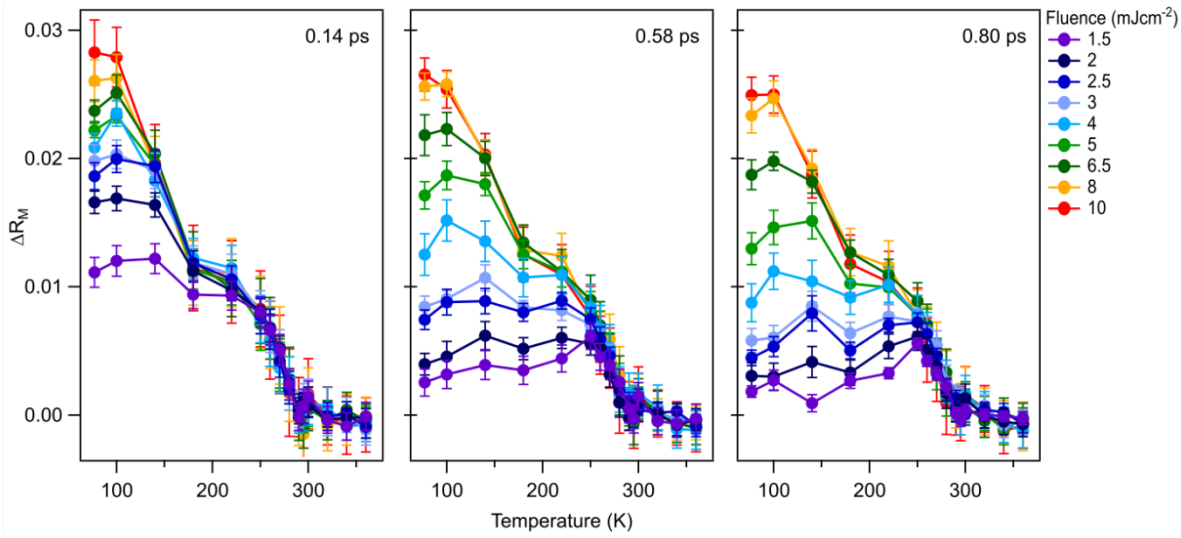

Figure S4 Temperature dependence of the magnetic degree of freedom (ΔR_M) at different excitation fluences measured at a time delay of 0.14 ps, 0.58 ps and 0.80 ps.

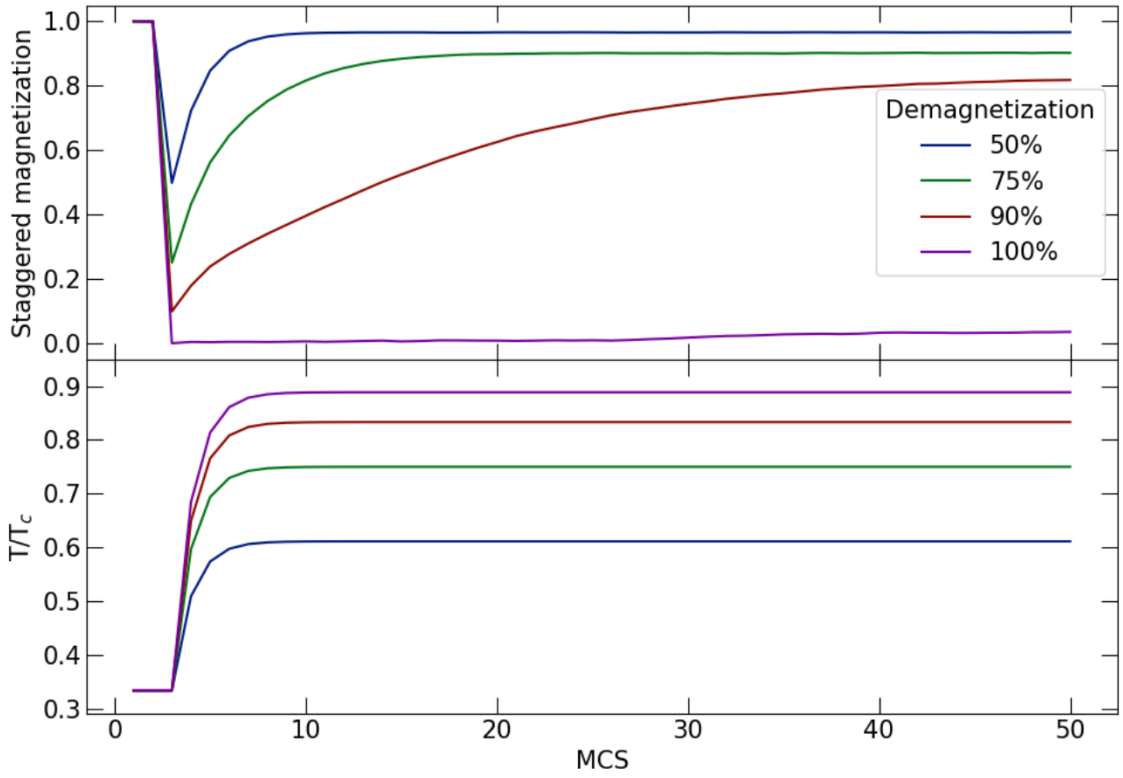

Figure S5 Magnetization dynamics (top) and temperature profile (bottom) of a Monte Carlo 3D spin-1/2 Ising model. Details on the simulation are discussed in the text.

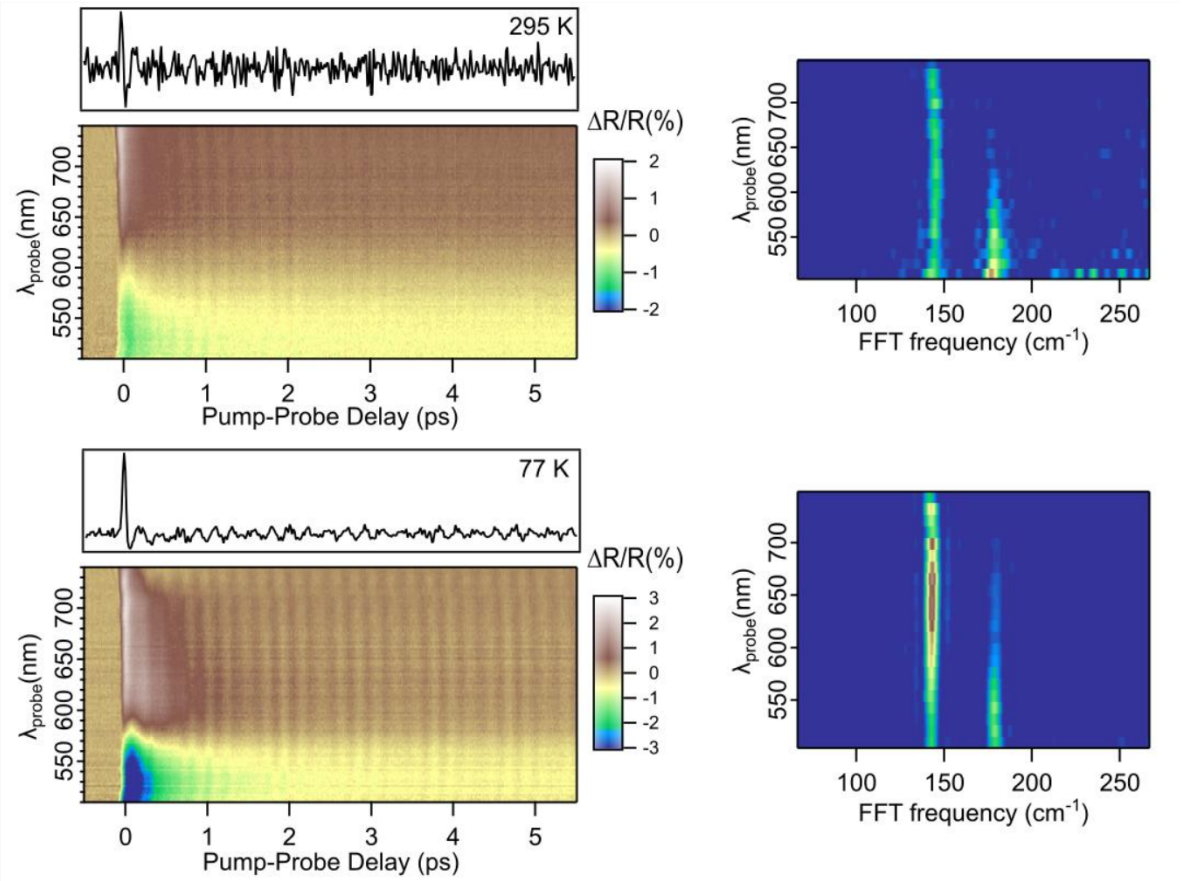

Figure S6 (left) Differentiation of the transient reflectivity change upon 800 nm excitation (F= 2.5 mJ cm^{-2}) at 295 K and 77 K. (right) Fourier transform of the oscillations in the transient reflectivity at 295 K and 77 K for each wavelength.